

Supplementary Information of

Trace amount of Ru-doped Ni-Fe oxide bone-like structures via single-step anodization: A flexible and bifunctional electrode for efficient overall water splitting

Moonsu Kim, Jaeyun Ha, Yong-Tae Kim, Jinsub Choi**

Department of Chemistry and Chemical Engineering
Inha University, 22212, Incheon, Republic of Korea

*To whom correspondence should be addressed.

Tel: +82-32-860-7476

e-mail: yongtaekim@inha.ac.kr, jinsub@inha.ac.kr

Index

1. Supplementary information

S1.1 Pore size distribution of NiFe-O@SS	
Figure S1	p.3
Figure S2	p.4
S1.2 Composition	
Figure S3	p.5
Figure S4	p.6
Table S1	p.7
S1.3 XPS analysis	
Figure S5	p.8
Figure S6	p.9
Figure S7	p.10
S1.4 Electrocatalytic property	
Table S2	p.11
Figure S8	p.11
S1.5 Electrochemical surface area	
Figure S9	p.12
Scheme S1	p.13
S1.6 Turnover frequency	
Table S3	p.14
S1.7 Operating full-cell with symmetric electrode settings	
Figure S10	p.16
S1.8 Stability	
Figure S11	p.17
Table S4	p.17
S1.9 Flexibility	
Figure S12	p.18
Figure S13	p.19
S1.10 Cost-effective material	
Figure S14	p.20
S1.11 Comparison of stainless steel-based electrodes	
Table S5	p.21
2. References	p.22

1. Supplementary information

S1.1 Pore size distribution of NiFe-O@SS

NiFe-O@SS prepared by anodization has a slightly ordered nanoporous structure. In general, the anodization process involves the following steps:

First, SS is oxidized by the positively biased potential ejecting Fe^{3+} ions into the electrolyte. The dissolved ferric ions react with fluoride ions at the interface between the SS and electrolyte, forming FeF_6^{3-} . Because they can dissolve in a small amount of water, the metal fluoride anions are etched away from the surface of the barrier oxide layer, thereby forming tiny pores within the oxide. Because the tip of the pores provides less resistance to the flow of current, the anodic reaction is focused at these sites, allowing the continuous growth of the porous metal oxide structure on the substrate¹. Under our experimental conditions, electric fields are produced with an applied voltage of 50 V at room temperature for 30 min. Anodic films on stainless steel, wherein a nano-structural film is formed directly on the substrate without a binder, serve as a catalyst with a physically and chemically stable support structure, an effective electron-transfer pathway, and a large surface area. The film comprises Fe and a small amount of Ni because the substrate is stainless steel.

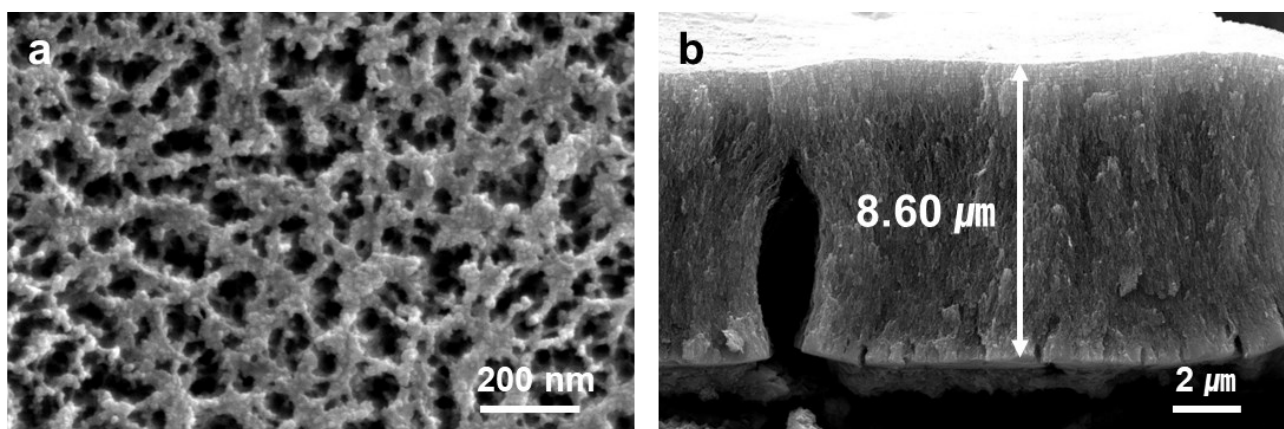


Figure S1. (a) Top and (b) cross-sectional SEM images of as-prepared NiFe-O@SS. The as-prepared film before annealing does not exhibit visible grains on the top surface.

NiFe-O@SS prepared from stainless steel 304 exhibits an ordered porous structure with an average pore size of 32.57 nm, which leads to a large aspect ratio in the structure.

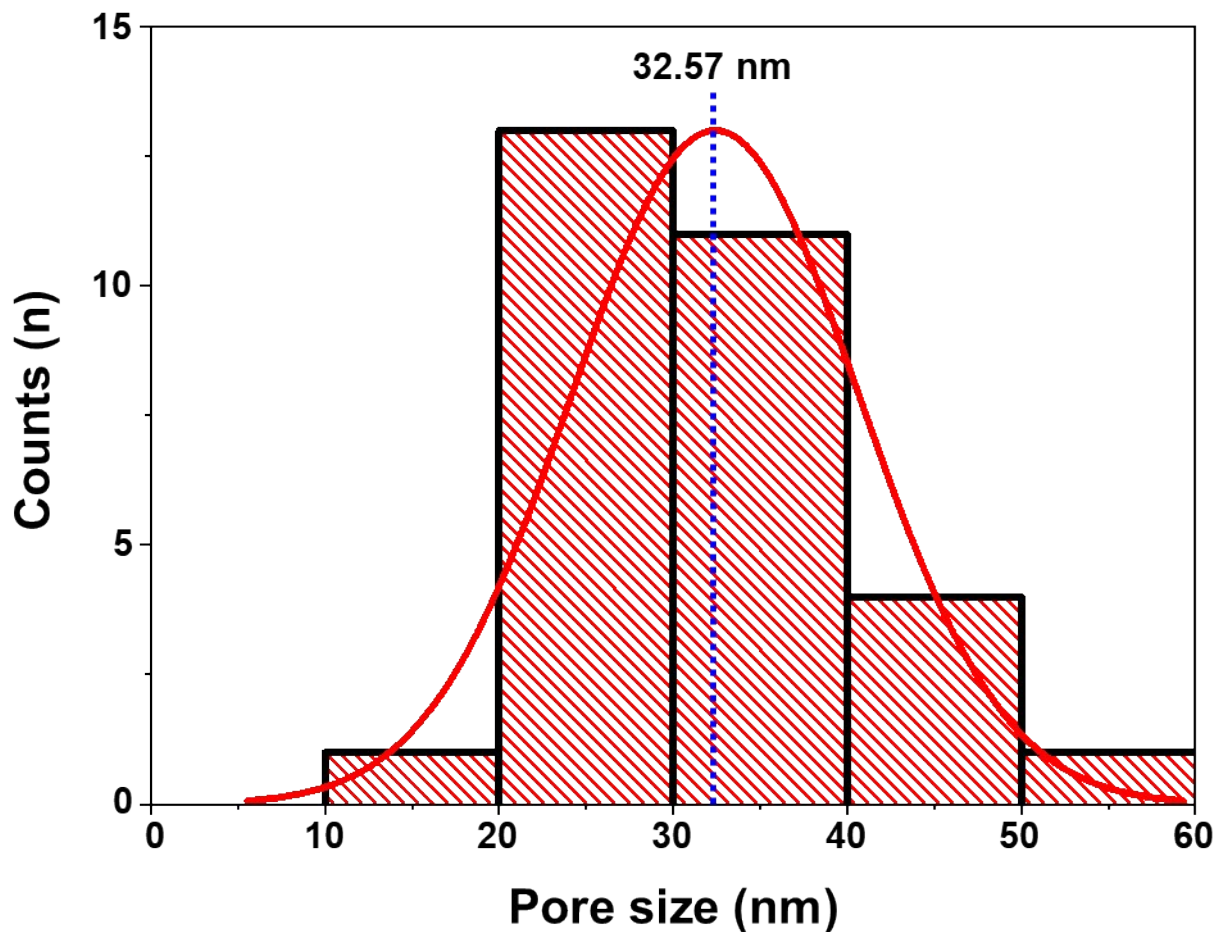


Figure S2. Pore size distribution curve of NiFe-O@SS.

S1.2 Composition

Information regarding the Ru concentration is obtained via the SEM and TEM-EDS images. Ru was doped into NiFe-O@SS at approximately 0.17 at% by a single-step anodization process.

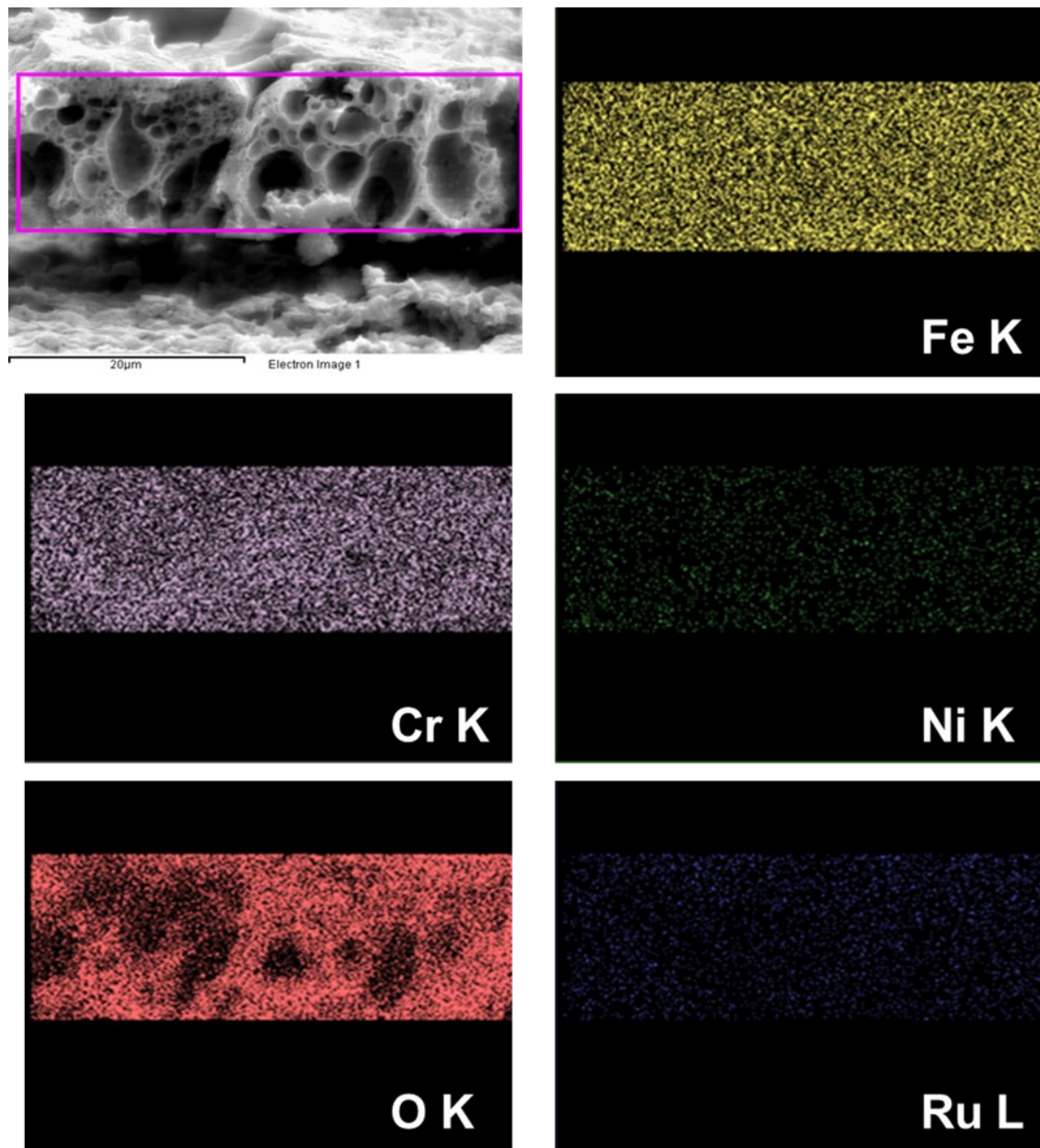


Figure S3. SEM-EDS images of RuNiFe-O@SS.

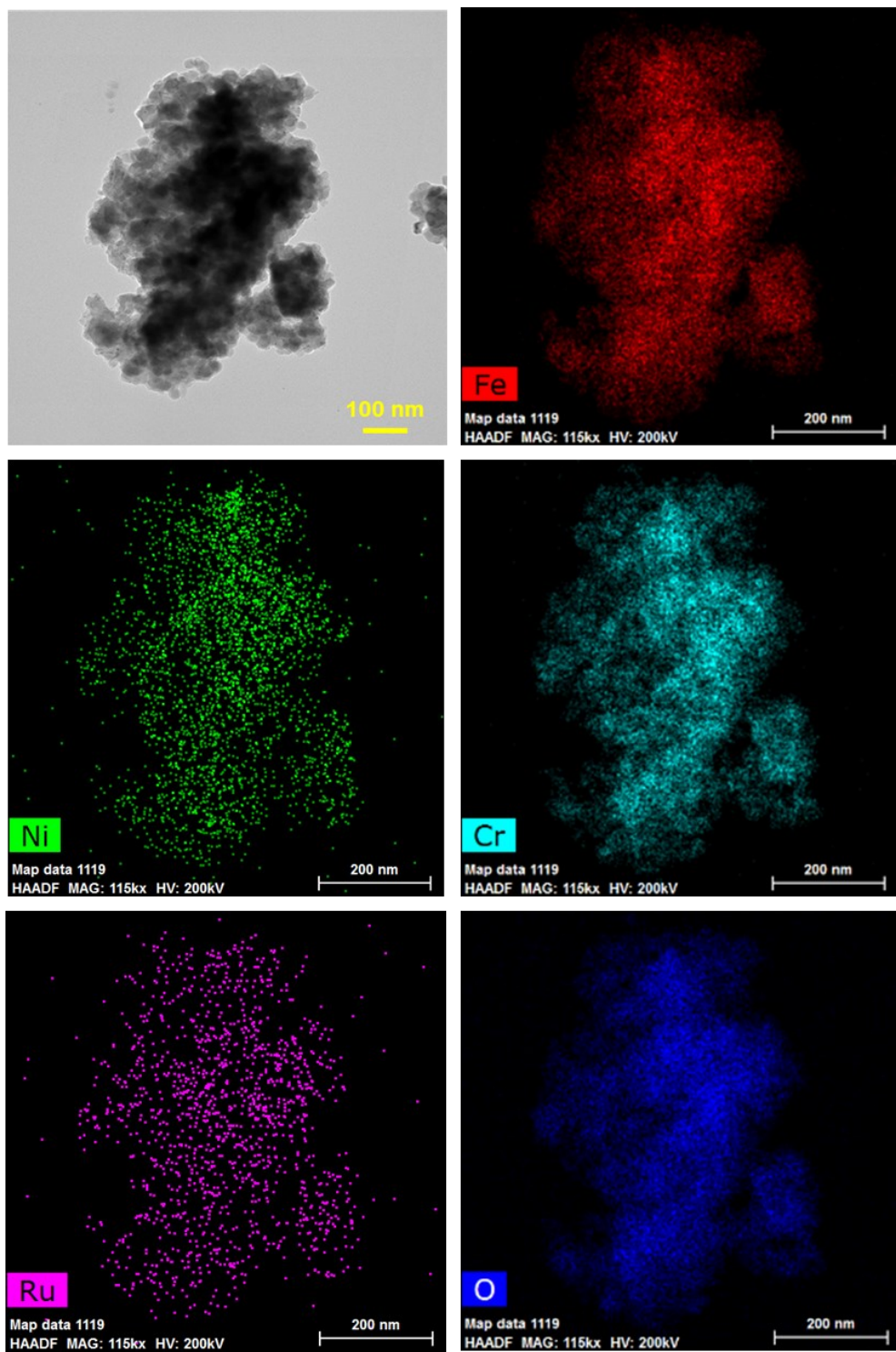


Figure S4. TEM-EDS images of RuNiFe-O@SS.

Table S1. Elemental compositions investigated by SEM and TEM-EDS.

Element	Result (SEM-EDS)		Result (TEM-EDS)	
	wt%	at%	wt%	at%
O K	36.85	66.62	30.65	60.08
Fe K	36.54	18.92	38.73	21.75
Cr K	23.12	12.86	28.13	16.97
Ni K	2.90	1.43	1.93	1.03
Ru L	0.58	0.17	0.56	0.17
Total	100			

S1.3 XPS analysis

Ru peaks in the RuNiFe-O@SS sample are not evident in the survey spectrum, because the Ru concentration is low and the Ru 3d peak is overlapped by the C 1s peak at the same energy. However, the high-resolution XPS spectrum shows a difference between the materials in the Ru 3d_{5/2} region.

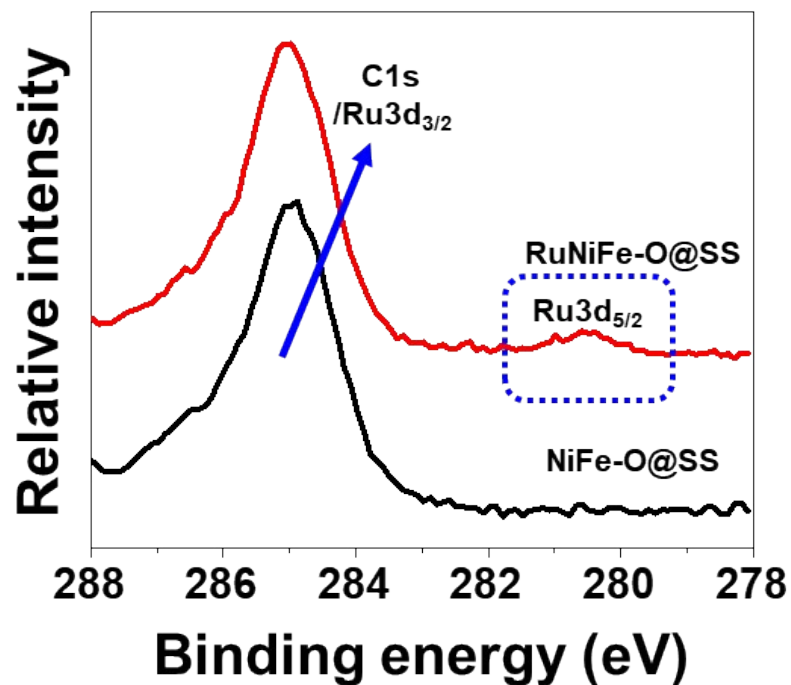


Figure S5. Comparative XPS spectra of NiFe-O@SS and RuNiFe-O@SS in the C 1s and Ru 3d regions.

NiFe-O@SS and RuNiFe-O@SS show highly similar spectral responses in the other regions. Fe 2p: 710.8 eV (Fe^{2+})^{1, 2}, 711.7 eV (Fe^{3+} , oxide), 713.9 eV (Fe^{3+} , hydroxide)³; Ni 2p: 855.2 eV (Ni^{2+} , oxide)⁴, 857.4 eV (Ni^{2+} , hydroxide)⁵; Cr 2p: 576.5 eV (Cr^{3+} , hydroxide)⁶, 577.0 eV (Cr^{3+} , oxide)^{1, 7}; O 1s: 530.1 eV (metal oxide)^{1, 8}, 532.2 eV (metal hydroxide and oxyhydroxide)⁹. However, RuNiFe-O@SS exhibits a response of low intensity at 529.6 eV in the O 1s spectrum, which is attributed to the RuO_x/Ru state^{10, 11}.

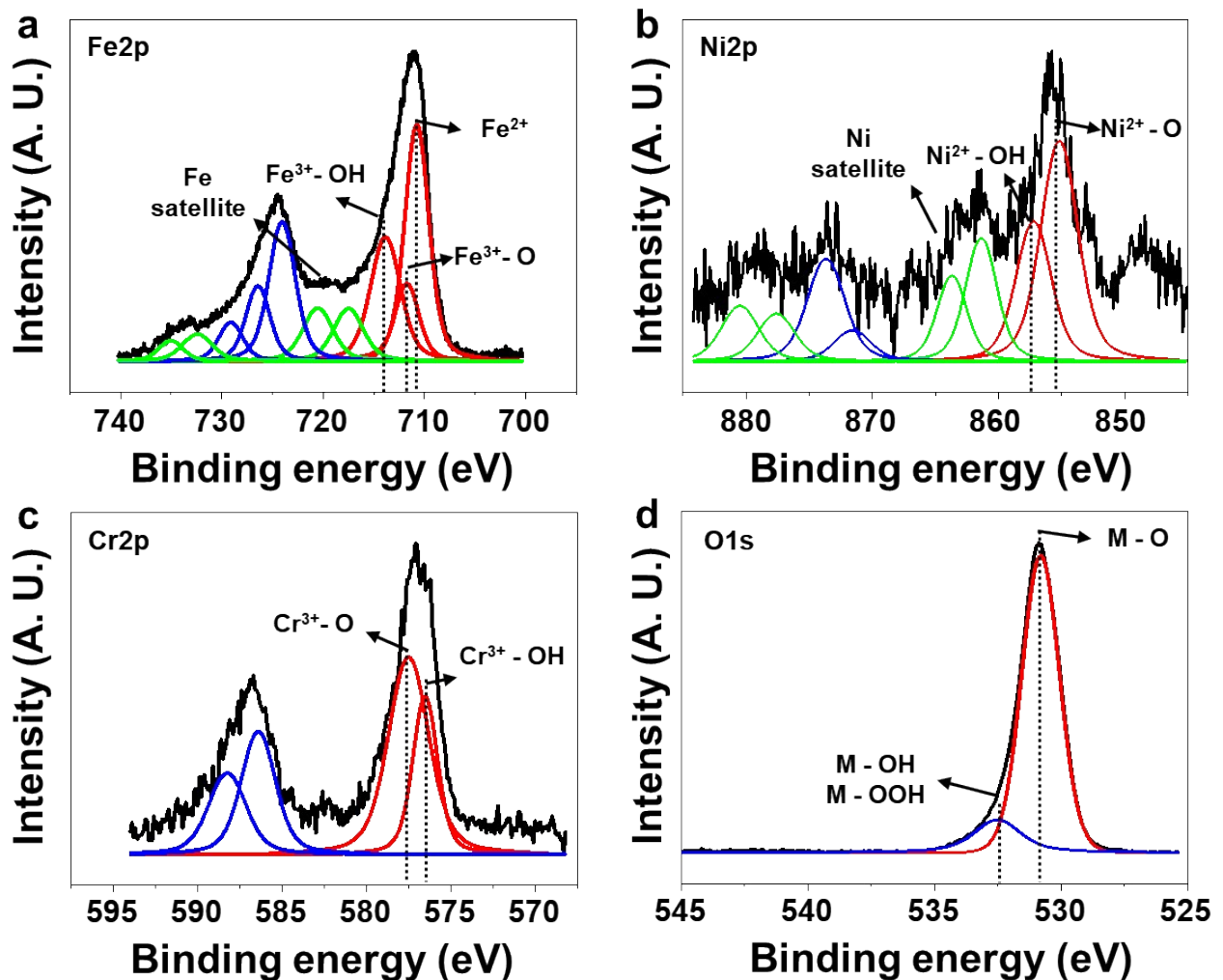


Figure S6. XPS spectra of NiFe-O@SS: (a) Fe 2p, (b) Ni 2p, (c) Cr 2p, and (d) O 1s.

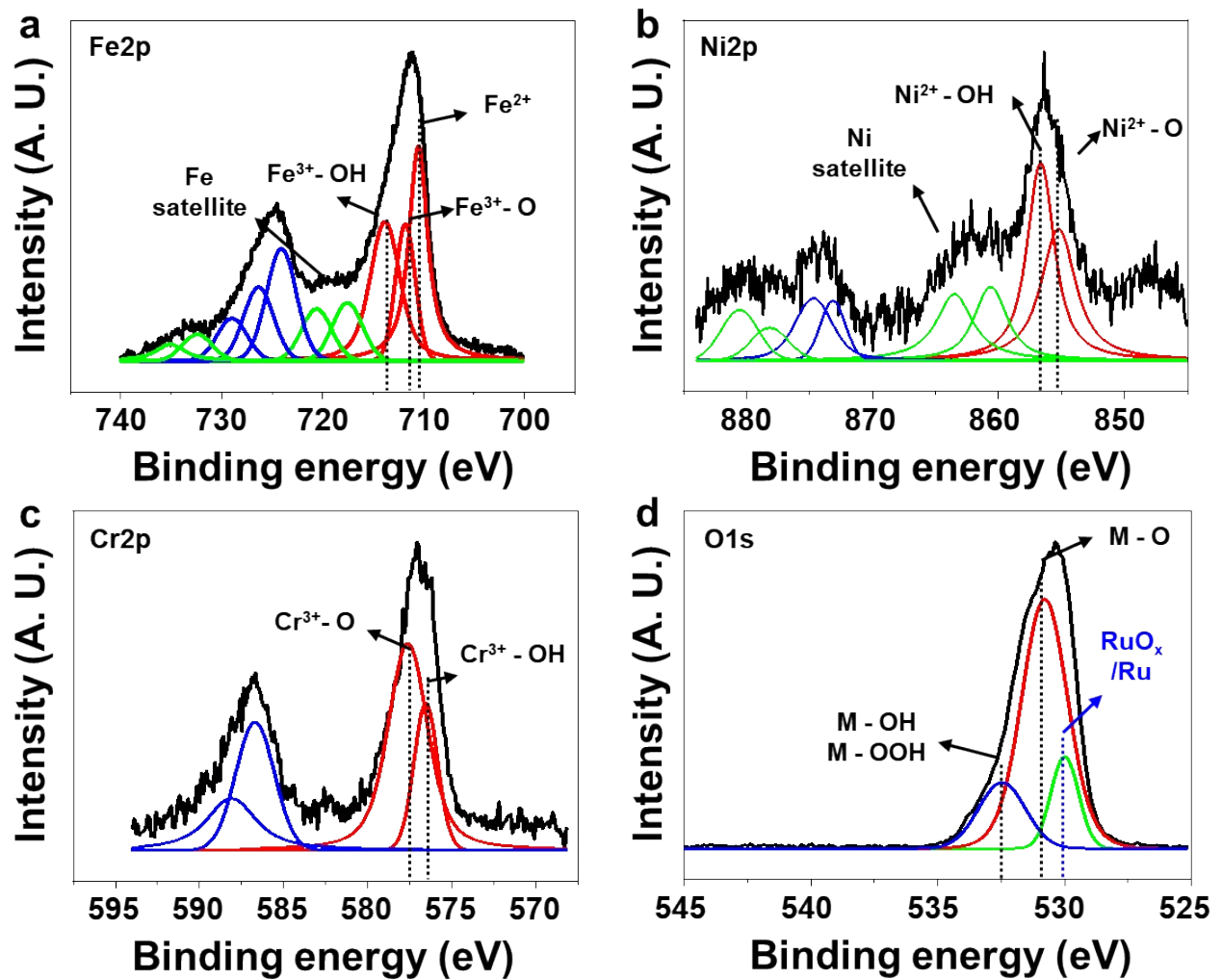


Figure S7. XPS spectra of RuNiFe-O@SS: (a) Fe 2p, (b) Ni 2p, (c) Cr 2p, and (d) O 1s.

S1.4 Comparison of electrochemical catalytic properties

Table S2. Electrocatalytic property value

	Tafel slope (mV dec ⁻¹)	j_0 ($\mu\text{A cm}^{-2}$)	Faradaic efficiency (%)	Ref.
WO ₃ -TiO ₂ -NiP	98	0.62	-	[12]
NiCu MMO	120	10.0	-	[13]
Ni _{0.9} Co _{0.1}	125	7.2	-	[14]
Ni@SS	135	0.29	-	[15]
Co@SS	108	0.16	-	
CoMn ₂ O ₄ spinel	62	-	95.06	[16]
CoMoS ₄ @NF	52	-	99	[17]
Modified SS316	147	-	100	[18]
Co ₂ P	52	-	80	[19]
Bare SS	114	0.07	-	This work
RuNiFe-O@SS	107	8.1	99	

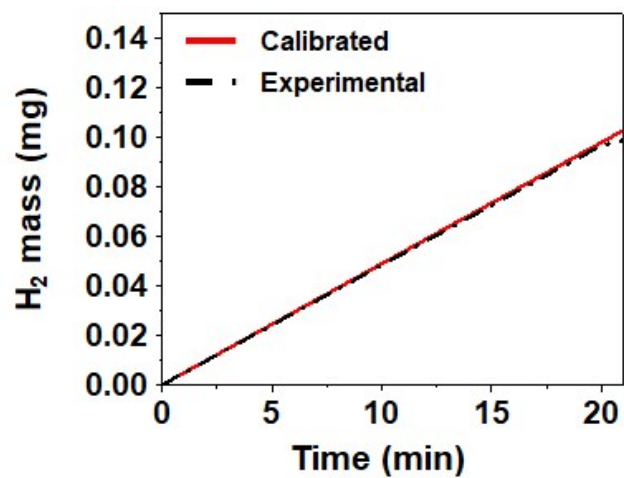


Figure S8. Faradaic efficiency of hydrogen evolution on the RuNiFe-O@SS.

S1.5 Electrochemical surface area

The electrochemical surface area (ECSA) is a typical criterion for establishing the active surface area of an electrode. Determination of the active surface area of the samples is depicted in Figure S8, including information regarding the active site and surface area.

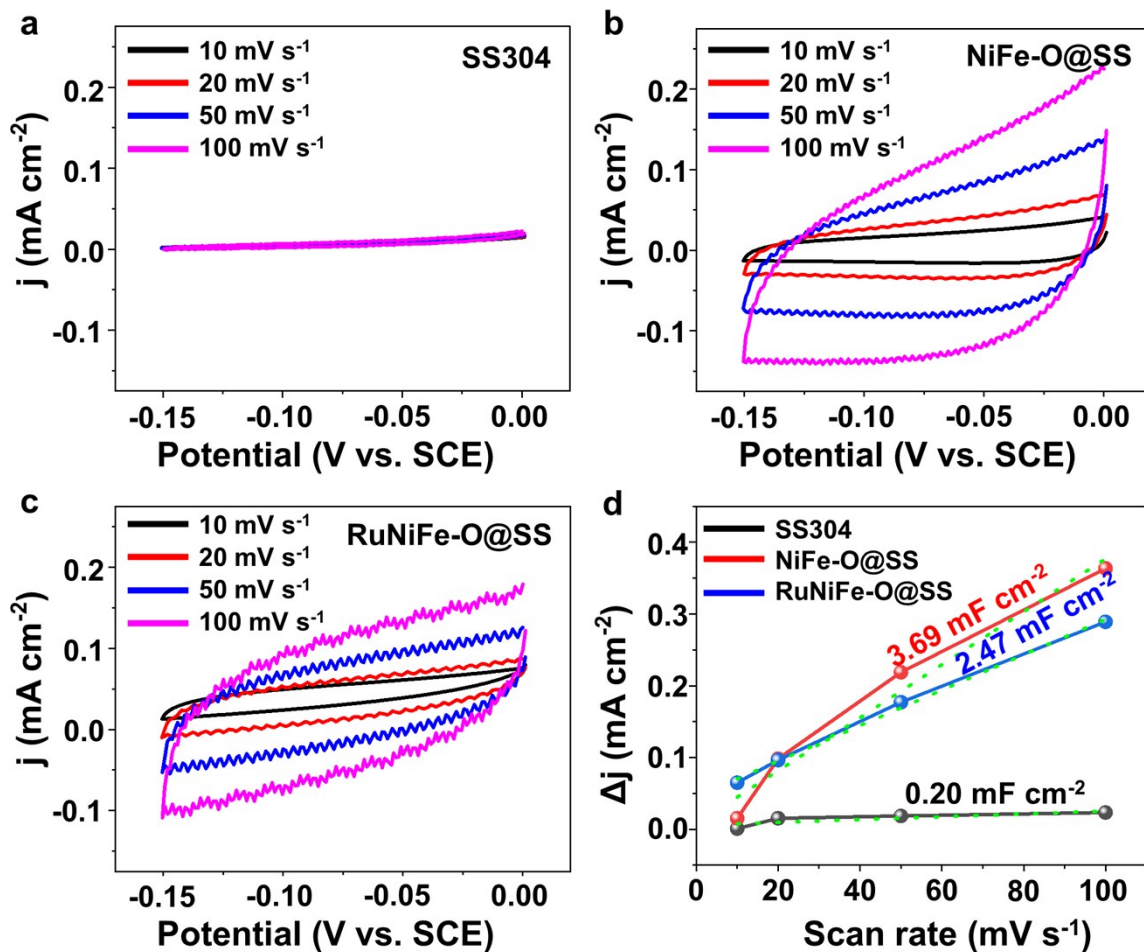
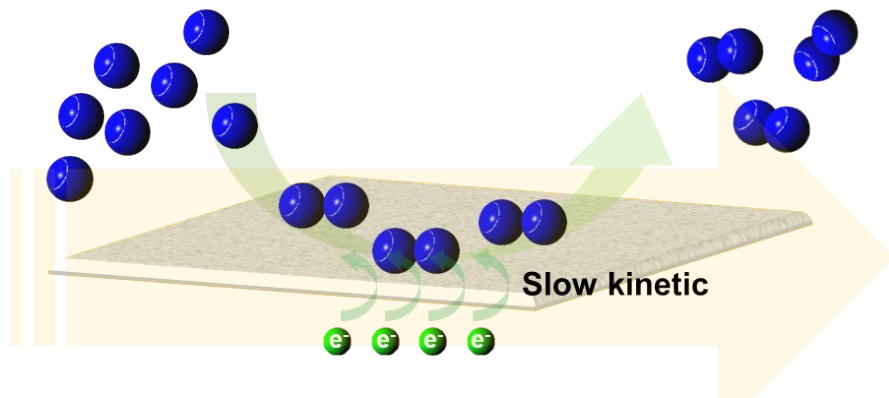


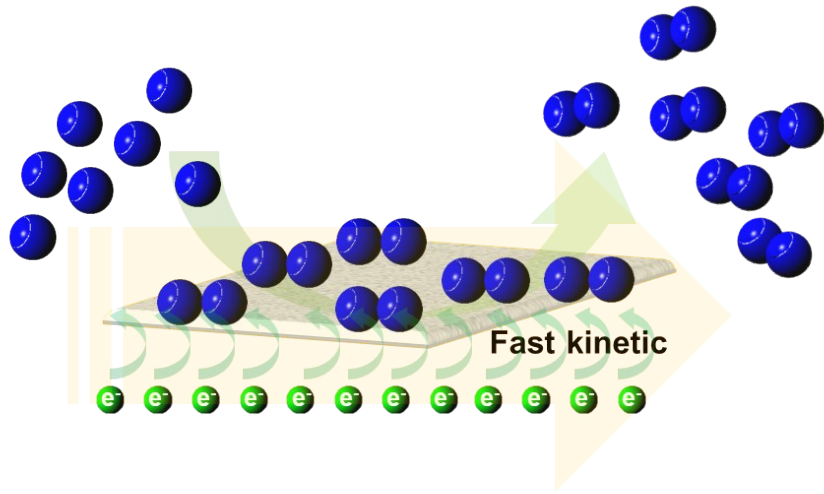
Figure S9. Cyclic voltammetric curves of (a) SS, (b) NiFe-O@SS, and (c) RuNiFe-O@SS at different scan rates in the non-faradaic region. (d) ECSA calculated from the cyclic voltammetric curves.

a



Larger surface area/ slow kinetic
/ narrow channel (not good mass transfer)

b



Smaller surface area/ fast kinetic
/ larger channel (good mass transfer)

Scheme S1. Illustrations correlating water-splitting performance with the active surface area and ease of mass transfer: (a) NiFe-O@SS and (b) RuNiFe-O@SS.

S1.6 Turnover frequency

The turnover frequency (TOF) was calculated using LSV and ECSA via the following procedure²⁰,²¹:

Table S3. Double layer capacitance and ECSA for SS, NiFe-O@SS, and RuNiFe-O@SS.

Electrocatalysts	SS	NiFe-O@SS	RuNiFe-O@SS
C _{dl} (mF cm ⁻²)	0.20	3.69	2.47
A _{ECSA} (cm ²)	1	18.45	12.35

The TOF was calculated using **equation S1**²²:

$$\text{TOF (s}^{-1}\text{)} = (\text{j} \times \text{N}_\text{A}) / (\text{n} \times \text{m} \times \text{F} \times \text{A}_\text{ECSA}) \quad (\text{S1})$$

where j, N_A, n, m, and F are the current density at a specific voltage, Avogadro's number (6.022×10^{23} mol⁻¹), number of electrons in the reaction (for HER, n = 2; for OER, n = 4), number of active sites, and Faraday constant (96,485 C mol⁻¹), respectively. The number of electrocatalytically active sites, m, which is based on a small amount of metal-doped magnetite (Fe₃O₄, PDF card No. # 19–0629), is calculated using the following description. Because the radii of Ru and Ni are similar to the radius of Fe, it is assumed that substitutional doping occurs in the following calculation²³.

Ratio of Fe : Ni : Ru = 128 : 6 : 1

Fe₃O₄ unit cell: Z = 8, Volume = 591.9 Å³; Containing 6 Fe and 8 O atoms

By ratio: Fe 5.69, Ni 0.27, Ru 0.04 per unit cell

Active sites of Fe_{2.85}Ni_{0.13}Ru_{0.02}O₄ = [(14 atoms)/(591.9 Å³)]^{2/3} per unit cell
 $= 8.628 \times 10^{14}$ atoms cm⁻²,_{real}

The TOF is calculated using **equation S2**,

$$\text{TOF (s}^{-1}\text{)} = (7.234 \times 10^3 \times j) / (n \times A_{\text{ECSA}}), \quad (\text{S2})$$

and presented in **Figure 5**.

S1.7 Operating full-cell with symmetric electrode settings

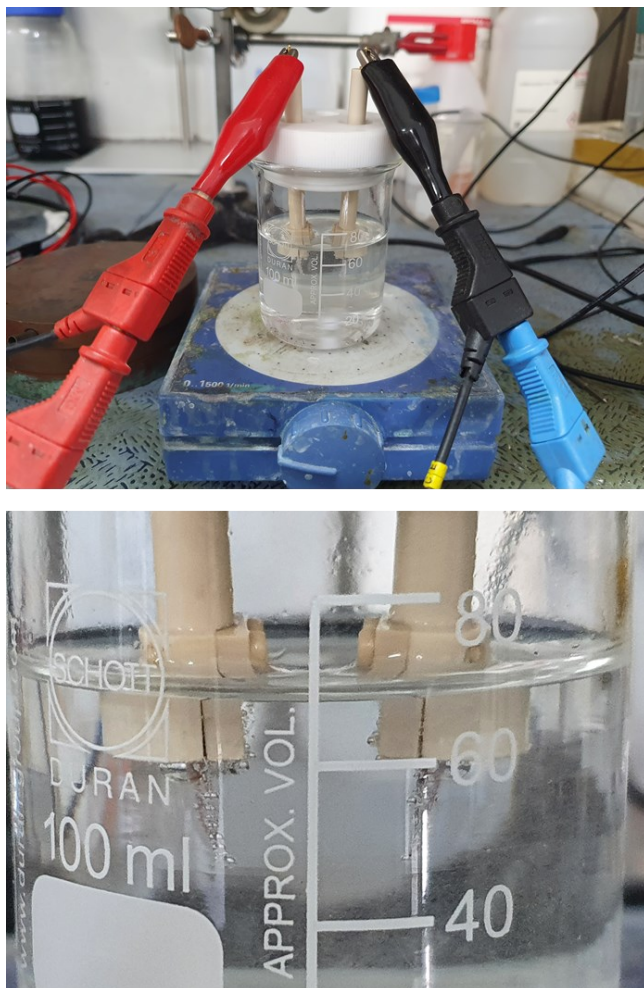


Figure S10. Photographs of homemade cell for water splitting. The rear of the naked SS substrate was covered with masking tape.

S1.8 Stability

After operating symmetrical electrolysis cell with a couple of bifunctional RuNiFe-O@SS electrodes, the morphology of the electrode was maintained with no remarkable alternation except for slight grain aggregation, which was generally developed in alkaline electrolyte.

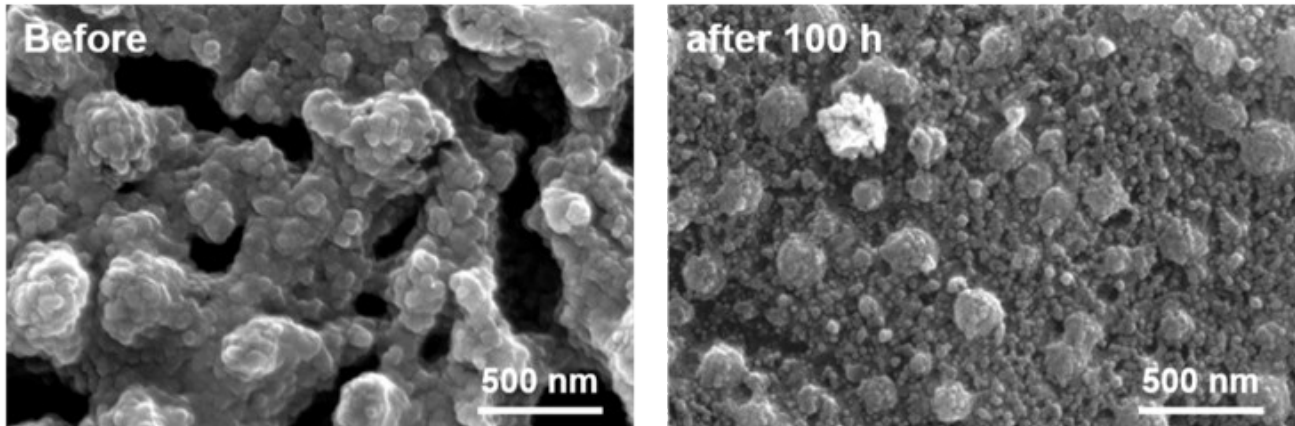


Figure S11. SEM images of RuNiFe-O@SS before and after chronopotentiometric measurements at 100 mA cm^{-2} for 100 h

In addition, The ICP-MS measurement indicates that no dissolution of electrode to electrolyte occurs during alternative chronopotentiometric measurements at 100 mA cm^{-2} for 100 h.

Table S4. ICP-MS measurement: concentration of Fe, Cr, Ni, and Ru ions after chronopotentiometric measurements at 100 mA cm^{-2} for 100 h.

Contents	Fe	Cr	Ni	Ru
Conc. (ppm)	0.439	1.253	0	0.363

S1.9 Flexibility

When the samples were folded and defolded several times, only RuNiFe-O@SS was restored because of its flexibility; in contrast, the NiFe-O@SS film cracked.

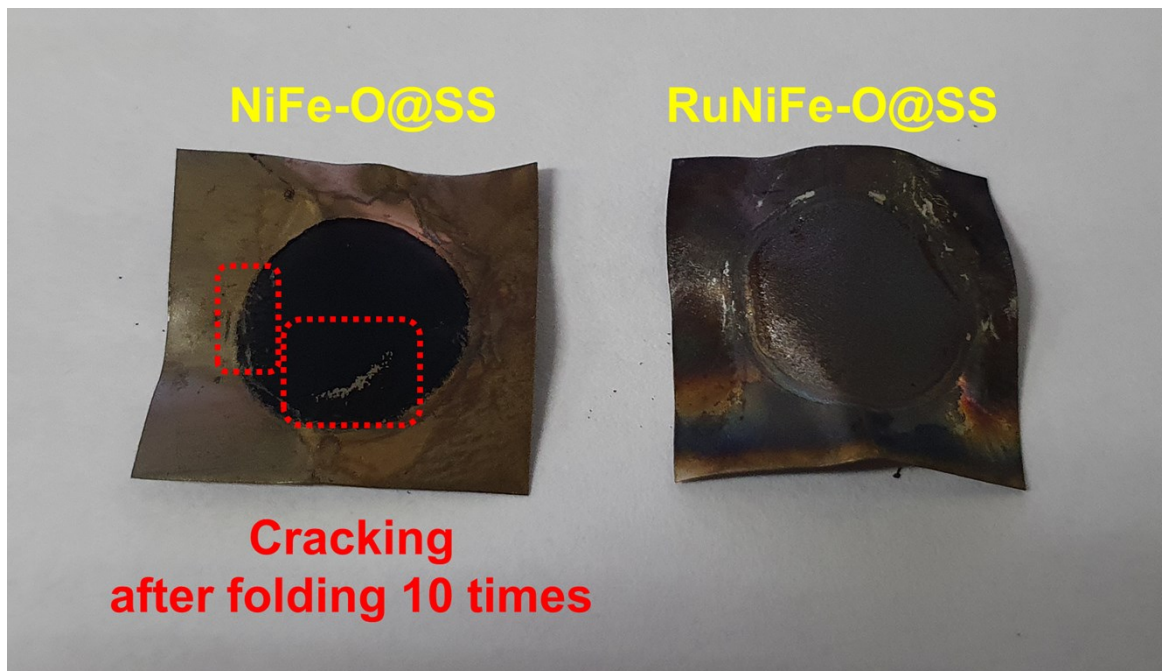


Figure S12. Photographs of the samples after folding and defolding.

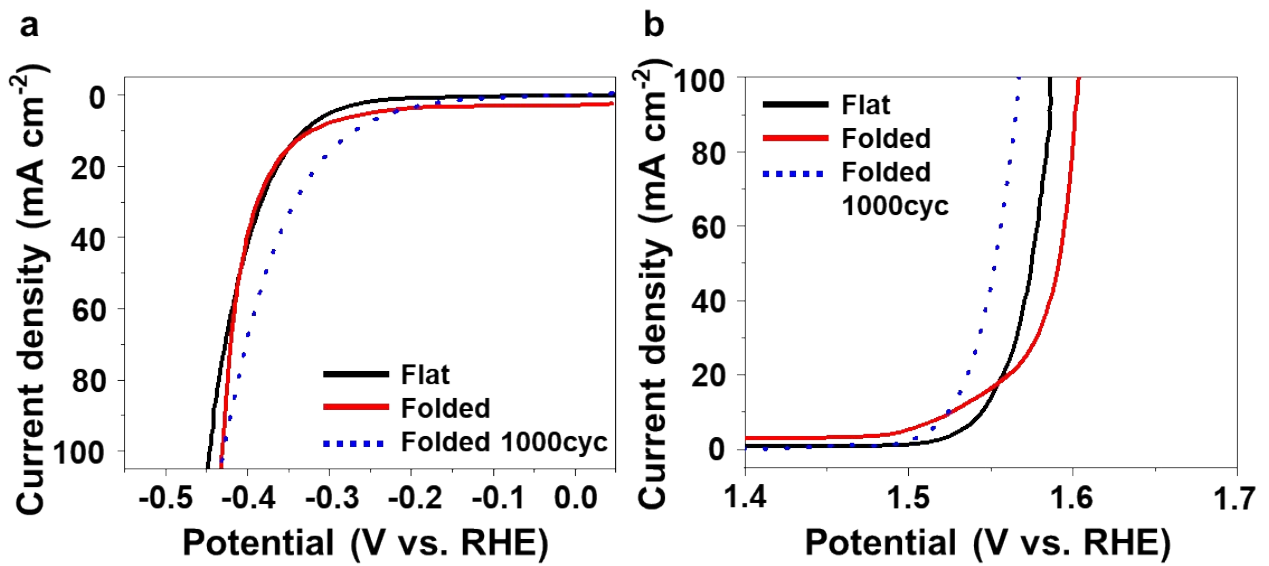


Figure S13. Electrocatalytic performance for HER and OER after folding and defolding.

S1.10 Cost-effective material

Stainless steel-based water splitting electrode is most promising cost-effective material²⁴. Therefore, these electrodes can be immediately used for industrial application with more cost-effective advantage than the other materials such as IrO₂-RuO₂ DSA (Figure S11), because relative cost of the electrode material of stainless steel-based material is extremely lower (relative cost: 0.00012) than Pt/C (relative cost: 32.52, HER side), and RuO₂ (relative cost: 12.35, OER side).

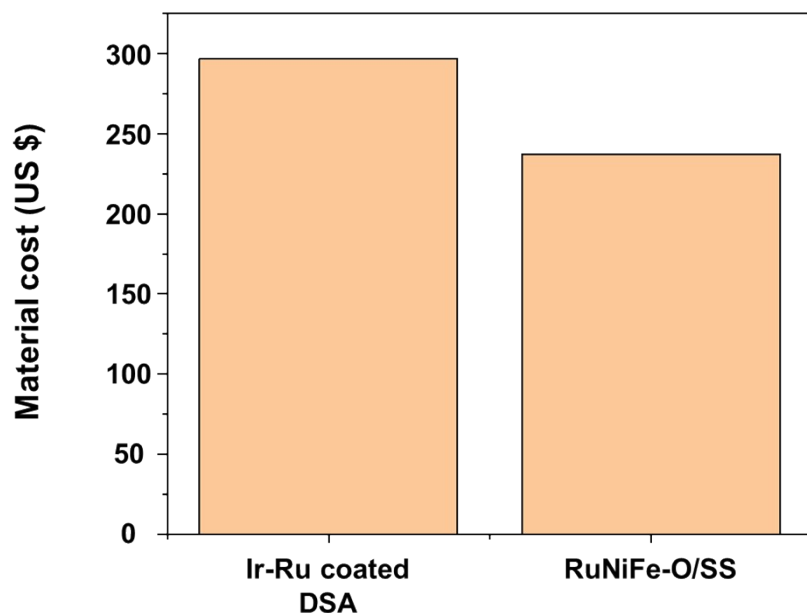


Figure S14. Comparison of the material cost between conventional DSA and RuNiFe-O/SS.

S1.11 Comparison

Table S5. Comparison of RuNiFe-O@SS with the other stainless steel-based electrodes.

Material	η_{HER} (mV)	η_{OER} (mV)	Tafel slope (HER, mV dec ⁻¹)	Tafel slope (OER, mV dec ⁻¹)	Ref.
SS scrubber	380 @ 50 mA cm ⁻²	418 @ 10 mA cm ⁻²	121	63	[24]
Bare SS304	627 @ 10 mA cm ⁻²	-	107	-	
Hard anodized SS	466 @ 10 mA cm ⁻²	-	58	-	[25]
Anodized Ni	-	340 @ 10 mA cm ⁻²	-	137	
NiFe = 0.12:0.88 alloy	-	380 @ 10 mA cm ⁻²	-	52	[26]
SS-304-Ox-ECA	426 @ 100 mA cm ⁻²	-	90	-	[27]
Ni42 steel	333 @ 10 mA cm ⁻²	-	72	-	[28]
Fe	360 @ 10 mA cm ⁻²	-	-	-	[29]
Modified S235	-	347 @ 2 mA cm ⁻²	-	58.5	[30]
Ru-doped anodized SS304	448 @ 100 mA cm ⁻²	353 @ 100 mA cm ⁻²	107	46 (@ 10 mA cm ⁻²) / 47 (@ 100 mA cm ⁻²)	This work

2. References

- 1 M. Kim, J. Ha, N. Shin, Y. -T. Kim, J. Choi, *Electrochim. Acta*, 2020, **364**, 137315. DOI: <https://doi.org/10.1016/j.electacta.2020.137315>.
- 2 L. Martinez, D. Leinen, F. Martín, M. Gabas, J. R. Ramos-Barrado, E. Quagliata, E. A. Dalchiele, *J. Electrochem. Soc.*, 2007, **154**, D126-D133. DOI: <https://doi.org/10.1149/1.2424416>.
- 3 P. M. Hallam, M. Gómez-Mingot, D. K. Kampouris, C. E. Banks, *RSC Adv.*, 2012, **2**, 6672-6679. DOI: <https://doi.org/10.1039/C2RA01139E>.
- 4 H. -Q. Wang, X. -P. Fan, X. -H. Zhang, Y. -G. Huang, Q. Wu, Q. -C. Pan, Q. -Y. Li, *RSC Adv.*, 2017, **7**, 23328-23333. DOI: <https://doi.org/10.1039/C7RA02932B>.
- 5 P. Ganesan, A. Sivanantham, S. Shanmugam, *J. Mater. Chem. A*, 2016, **42**, 16394-16402. DOI: <https://doi.org/10.1039/C6TA04499A>.
- 6 T. Zhang, Y. Han, W. Wang, Y. Gao, Y. Song, X. Ran, *Acta Metall. Sin. (Engl. Lett.)*, 2020, **33**, 1289-1301. DOI: <https://doi.org/10.1007/s40195-020-01049-5>.
- 7 A. S. Kilian, F. Bernardi, A. Pancotti, R. Landers, A. de Siervo, J. Morais, *J. Phys. Chem. C*, 2014, **118**, 20452-20460. DOI: <https://dx.doi.org/10.1021/jp506507e>.
- 8 S. Y. Turishchev, O. A. Chuvenkova, E. V. Parinova, D. A. Koyuda, R. G. Chumakov, M. Presselt, A. Schleusener, V. Sivakov, *Results Phys.*, 2018, **11**, 507-509. DOI: <https://doi.org/10.1016/j.rinp.2018.09.046>.
- 9 R. Xiang, C. Tong, Y. Wang, L. Peng, Y. Nie, L. Li, X. Huang, Z. Wei, *Chinese J. Catal.*, 2018, **39**, 1736-1745. DOI: [https://doi.org/10.1016/S1872-2067\(18\)63150-X](https://doi.org/10.1016/S1872-2067(18)63150-X).
- 10 J. Y. Shen, A. Adnot, S. Kaliaguine, *Appl. Surf. Sci.*, 1991, **51**, 47-60. DOI: [https://doi.org/10.1016/0169-4332\(91\)90061-N](https://doi.org/10.1016/0169-4332(91)90061-N).
- 11 C. Mun, J. J. Ehrhardt, J. Lambert, C. Madic, *Appl. Surf. Sci.*, 2007, **253**, 7613-7621. DOI: <https://doi.org/10.1016/j.apsusc.2007.03.071>.
- 12 V. R. Anupama, A. S. Mideen, S. M. A. Shibli, *Int. J. Hydrogen Energy*, 2021, **In press**. DOI: <https://doi.org/10.1016/j.ijhydene.2021.02.107>.

- 13 A. Y. Faid, A. O. Barnett, F. Seland, S. Sunde, *Electrochim. Acta*, 2021, **371**, 137837. DOI: <https://doi.org/10.1016/j.electacta.2021.137837>.
- 14 M. J. Gomez, E. A. Franceschini, G. I. Lacconi, *Electrocatalysis*, 2018, **9**, 459-470. DOI: <https://doi.org/10.1007/s12678-018-0463-5>.
- 15 C. Fan, D. L. Piron, A. Slep, P. Paradis, *J. Electrochem. Soc.*, 1994, **141**, 382-387. DOI: <https://doi.org/10.1149/1.2054736>.
- 16 J. Lee, N. Son, N. -K. Park, H. -J. Ryu, J. -I. Baek, Y. Sohn, J. Y. Do, M. Kang, *Electrochim. Acta*, 2021, **379**, 138168. DOI: <https://doi.org/10.1016/j.electacta.2021.138168>.
- 17 A. A. Yadav, Y. M. Hunge, S. -W. Kang, *Ultrason. Sonochem.*, 2021, **72**, 105454. DOI: <https://doi.org/10.1016/j.ultsonch.2020.105454>
- 18 X. Liu, B. You, Y. Sun, *ACS Sustainable Chem. Eng.*, 2017, **5**, 4778-4784. DOI: <https://doi.org/10.1021/acssuschemeng.7b00182>.
- 19 Z. Jin, P. Li, D. Xiao, *Green Chem.*, 2016, **18**, 1459-1464. DOI: <https://doi.org/10.1039/C5GC02462E>.
- 20 Y. Wang, T. Williams, T. Gengenbach, B. Kong, D. Zhao, H. Wang, C. Selomulya, *Nanoscale*, 2017, **9**, 17349-17356. DOI: <https://doi.org/10.1039/C7NR06186B>.
- 21 H. Zhao, Z. Li, X. Dai, M. Cui, F. Nie, X. Zhang, Z. Ren, Z. Yang, Y. Gan, X. Yin, Y. Wang, W. Song, *J. Mater. Chem. A*, 2020, **8**, 6732-6739. DOI: <https://doi.org/10.1039/C9TA13553G>.
- 22 J. Benson, M. Li, S. Wang, P. Wang, P. Papakonstantinou, *ACS Appl. Mater. Interfaces*, 2015, **7**, 14113-14122. DOI: <https://doi.org/10.1021/acsami.5b03399>.
- 23 L. H. Ahrens, *Geochim. Cosmochim. Acta*, 1952, **2**, 155-169. DOI: [https://doi.org/10.1016/0016-7037\(52\)90004-5](https://doi.org/10.1016/0016-7037(52)90004-5).
- 24 S. Anantharaj, S. Chatterjee, K. C. Swaathini, T. S. Amarnath, E. Subhashini, D. K. Pattanayak, S. Kundu, *ACS Sustainable Chem. Eng.*, 2018, **6**, 2498-2509. DOI: <https://doi.org/10.1021/acssuschemeng.7b03964>.
- 25 M. Kim, Y. -T. Kim, J. Choi, *Electrochim. Commun.*, 2020, **117**, 106770. DOI: <https://doi.org/10.1016/j.elecom.2020.106770>.

- 26 N. Yamada, S. Kitano, Y. Yato, D. Kowalski, Y. Aoki, H. Habazaki, *ACS Appl. Energy Mater.*, 2020, **3**, 12316-12326. DOI: <https://dx.doi.org/10.1021/acsaem.0c02362>.
- 27 S. Anantharaj, H. Sugime, S. Noda, *ACS Appl. Energy Mater.*, 2020, **3**, 12596-12606. DOI: <https://dx.doi.org/10.1021/acsaem.0c02505>.
- 28 H. Schäfer, D. M. Chevrier, P. Zhang, J. Stangl, K. M.-Buschbaum, J. D. Hardege, K. Kuepper, J. Wollschläger, U. Krupp, S. Dühnen, M. Steinhart, L. Walder, S. Sadaf, M. Schmidt, *Adv. Func. Mater.*, 2016, **26**, 6402-6417. DOI: <https://doi.org/10.1002/adfm.201601581>.
- 29 B. C. M. Martindale, E. Reisner, *Adv. Energy Mater.*, 2016, **6**, 1502095-1502103. DOI: <https://doi.org/10.1002/aenm.201502095>.
- 30 H. Schäfer, K. Kuepper, J. Wollschläger, N. Kashaev, J. D. Hardege, L. Walder, S. M. B.-Mousavi, B. H.-Azanza, M. Steinhart, S. Sadaf, F. Dorn, *ChemSusChem*, 2015, **8**, 3099-3110. DOI: <https://doi.org/10.1002/cssc.201500666>.